

## CALSPEC: WFC3 IR GRISM SPECTROPHOTOMETRY

RALPH C. BOHLIN<sup>1</sup>, AND SUSANA E. DEUSTUA<sup>1</sup>

<sup>1</sup>Space Telescope Science Institute, 3700 San Martin Drive, Baltimore, MD 21218, USA

### ABSTRACT

The collections of spectral energy distributions (SEDs) in the *Hubble Space Telescope* (HST) CALSPEC database are augmented by 19 IR SEDs from Wide Field Camera 3 (WFC3) IR grism spectra. Together, the two IR grisms, G102 and G141, cover the 0.8–1.7  $\mu\text{m}$  range with resolutions  $R=200$  and 150, respectively. These new WFC3 SEDs overlap existing CALSPEC Space Telescope Imaging Spectrograph (STIS) standard star flux distributions at 0.8–1  $\mu\text{m}$  with agreement to  $\lesssim 1\%$ . Some CALSPEC standards already have near-IR camera and multi-object spectrograph (NICMOS) SEDs; but in their overlap region at 0.8–1.7  $\mu\text{m}$ , the WFC3 data have better wavelength accuracy, better spectral resolution, better repeatability, and, consequently, better flux distributions of  $\sim 1\%$  accuracy in our CALSPEC absolute flux SEDs vs.  $\sim 2\%$  for NICMOS. **With the improved SEDs in the WFC3 range, the modeled extrapolations to 32  $\mu\text{m}$  for JWST flux standards begin to lose precision longward of the 1.7  $\mu\text{m}$  WFC3 limit, instead of at the 1.0  $\mu\text{m}$  long wavelength limit for STIS. For example, the extrapolated IR flux longward of 1.7  $\mu\text{m}$  for 1808347 increases by  $\sim 1\%$  for the model fit to the data with WFC3, instead of just to the STIS SED alone.**

*Keywords:* stars: atmospheres — stars: fundamental parameters — techniques: spectroscopic — infrared: stars

### 1. INTRODUCTION

Absolute flux distributions of standard stars with pedigrees traceable to the International System of Units (SI) are essential for 21st century astrophysics and precision cosmology. For example, dark energy investigations that rely on observations of Type Ia supernovae (SNe Ia) require an absolute color calibration, i.e. band-to-band, with an accuracy of better than 1% (Scolnic et al. 2014; Stubbs & Brown 2015). JWST, WFIRST and other future large space telescopes, along with large ground-based projects like PanSTARRS and LSST, need reliable flux standard stars with a wide range of brightness over the whole sky (Stubbs & Tonry 2016).

Stellar-flux uncertainty requirements are driven in part by the use of SNe Ia as probes of the expansion history of the universe. In 1998, the accelerating expansion of the universe was discovered, which implies the existence of a new component of the universe called dark energy. Cosmological and dark energy parameters are determined from the SNe Ia brightness-redshift relationship (Hubble diagram). To distinguish between competing dark energy models whose predictions differ by as little as 2% (Albrecht et al. 2006), dark energy investigations require sub-percent absolute spectral radiometric uncertainty and cross-calibration of the relative zero-points of all bands to an accuracy of better than 0.5% over the wavelength range of 0.48–2  $\mu\text{m}$ . Therefore, missions like WFIRST will depend upon a network of primary standard stars measured with absolute photometric uncertainty of better than 1% (0.01mag) over this range, which is an ambitious but achievable goal.

Although the motivation for sub-percent flux calibration accuracy is driven by cosmology, reducing the uncertainties in absolute stellar spectrophotometry benefits other research areas. The fundamental parameters of stars, including mass, radius, metallicity, and age, are inferred by matching accurate models of stellar atmospheres to calibrated spectroscopic data in order to determine the effective temperature, surface gravity, composition, and interstellar reddening. Model atmospheres for stars with relatively simple atmospheres, such as pure hydrogen white dwarfs, combine with stellar interior models to predict photometric parameters, stellar radii, and absolute luminosities. These results plus precise photometry predict stellar distances, which are in excellent agreement with measured trigonometric parallaxes (Holberg et al. 2008). When combined with GAIA’s exquisite astrometric accuracy, which yields parallaxes with uncertainties of 0.04–0.7 milliarcseconds for 1.5 billion stars, sub-percent spectrophotometry makes possible meaningful tests of 3-D spherical stellar models. Masses are directly calculated, and quantitative tests of evolutionary models are

improved.

Currently, the best choice of fundamental standards in the UV to near-IR are the CALSPEC models for the primary pure hydrogen white dwarfs (WDs) G191B2B, GD153, and GD71, which are the basis for the spectral energy distributions (SEDs) in the HST/CALSPEC<sup>1</sup> database. This paper specifies procedures required to place WFC3 IR grism SEDs on the CALSPEC absolute flux scale of Bohlin et al. (2014). Section 2 outlines the data processing steps required to extract photometric spectra from the WFC3 IR grism images. Section 3 details the correction for the changing sensitivity with time, while Section 4 compares WFC3 SEDs with the STIS results from CALSPEC in order to derive the WFC3 count rate non-linearity (CRNL) correction. Section 5 summarizes the absolute flux calibration of the WFC3 IR grisms; and in Section 6, the fully corrected WFC3 SEDs are compared with models to extend predictions of the flux distributions to 32  $\mu\text{m}$  for JWST calibration purposes.

## 2. DATA ANALYSIS

### 2.1. The Data

The publically available WFC3 IR grism observations of CALSPEC stars in the nominal Stare Mode include the white dwarf standard stars G191B2B, GD153, and GD71, plus sixteen other CALSPEC stars. These spectra were acquired at multiple locations on the IR detector. Grism Scanned Mode observations of CALSPEC stars will be discussed in a subsequent publication (Deustua & Bohlin, in prep). Table 1 itemizes the 19 WFC3 grism observations in Stare Mode, and indicates whether NICMOS observations are also available.

Table 1. WFC3 IR Observations of CALSPEC Stars

Star	CALSPEC Name	J <sup>a</sup>	Sp.Ty. <sup>a</sup>	G102 <sup>b</sup>	G141 <sup>b</sup>	NICMOS
2MASS J17571324+6703409	1757132	11.31	A3V	8	8	No
2MASS J18022716+6043356	1802271	11.87	A2V	6	8	Yes
2MASS J18083474+6927286	1808347	11.65	A3V	6	3	No
2MASS J00361617+1821104	2m003618	12.47	L3.5	2	2	Yes
2MASS J05591914-1404488	2m055914	13.80	T4.5	2	233	Yes
BD+60 1753	bd60d1753	9.61	A1V	8	8	No
2MASS J03323287-2751483	c26202	15.40	F8IV	0	4	Yes
G191B2B	g191b2b	12.54	DA.8	19	15	Yes
GD153	gd153	14.01	DA1.2	77	77	Yes
GD71	gd71	13.73	DA1.5	58	58	Yes
GRW+70°5824	grw_70d5824	13.25	DA2.4	26	27	Yes
HD37725	hd37725	7.95	A3V	1	0	No
2MASS J17583798+6646522	kf06t2	11.90	K1.5III	3	4	Yes
2MASS J16313382+3008465	p330e	11.77	G2V	8	13	Yes
2MASS J16194609+5534178	snap2	14.97	G0-5	1	2	Yes
VB8	vb8	9.78	M7V	2	2	Yes
WD1327-083	wd1327_083	12.62	DA3.5	2	2	No
WD1657+343	wd1657_343	...	DA.9	1	1	Yes
WD2341+322	wd2341_322	13.17	DA3.8	2	2	No

<sup>a</sup>J mag and Spectral Type are from Simbad

<sup>b</sup>Number of available WFC3 observations that are included in our average SEDs.

<sup>1</sup> <http://www.stsci.edu/hst/observatory/crds/calspec.html>

## 2.2. Extraction of Spectra from the Images

The software for producing files of flux vs. wavelength for the WFC3 IR grisms is an adaptation of similar code that was written by D. J. Lindler and utilized for the NICMOS grism data (Bohlin et al. 2005, 2006). Our procedure takes advantage of the zero order method (Bohlin et al. 2015). The first step is to locate the zero-order image and establish the wavelength scale. This method requires an accuracy of  $\sim 1''$  for the astrometry in the data file headers. In case the observer specified incorrect coordinates or omitted a significant proper motion, the target coordinates are updated in the input file headers.

If there is no zero order on the grism image, but there is an associated direct image, the (x,y) position of the star is found in the direct image. Then, the AXE method (Kuntschner et al. 2009a,b) is used with updated dispersion constants (Pirzkal et al. 2016) and wavelengths referenced to the stellar position on the direct image. In the rare case where neither a direct image nor a zero order is available, then the astrometry is often good enough to locate the spectrum, e.g. icqw01b1q for GD71, where a large wavelength correction of  $91 \text{ \AA}$  is required.

To establish the spectral trace to better precision than predicted by the astrometry, the image is searched for the -1, +1, and +2 orders. A linear least square fit to the (x,y) positions of the zero order and to any of the three spectral orders that are found determines the exact slope and location of the spectral trace. A discussion of the range of measured slopes appears in Bohlin et al. (2015).

After establishing the wavelength vector and spectral trace of the spectrum's position on the grism image, a scaled master sky background is subtracted to remove the structure in the vignettted sky background. Next, a wavelength-dependent flat-field data-cube (Deustua 2019, in prep) is applied to the relevant pixels in the image.

The final processing steps extract the gross spectrum with a height of six pixels ( $\sim 0.78''$ ) and subtract the residual background to produce the net stellar signal vector. The six pixel height is a trade-off between collecting more signal for bright stars and minimizing excess noise for faint sources. This choice includes 85-90% of the total signal (Kuntschner et al. 2009a,b). To maintain photometric accuracy with the relatively small height of six pixels, the spectral trace must be located with a precision of  $\lesssim 1$  pixel. Section 5 covers the absolute flux calibration.

The WFC3 IR grisms have dispersions of  $24.5 \text{ \AA}$  per pixel for G102 and  $46.5 \text{ \AA}$  per pixel for G141, and Bohlin et al. (2015) quote a wavelength precision of 5 and  $9 \text{ \AA}$  for G102 and G141, respectively. To verify the wavelength accuracy, a comparison of the SpeX spectrum of the brown dwarf star 2MASS J05591914-140448 (2M055914 in the CALSPEC database) with WFC3 IR is shown in Figure 1. The SpeX spectrum of (Burgasser et al. 2006) has a spectral resolution of  $\sim 150$  between 0.8 and 2.5 micron, comparable to WFC3 IR, and a wavelength precision of  $\pm 0.3 \text{ \AA}$  (Cushing et al. 2004). Figure 1 demonstrates that the WFC3/IR wavelength scale agrees with SpeX to within  $10 \text{ \AA}$ , while the NICMOS spectrum of the same source shows differences of up to  $40 \text{ \AA}$ . NICMOS used three grisms to cover the wavelength range between 0.8 to  $2.5 \mu\text{m}$  with dispersions of 50-100  $\text{ \AA}$  per pixel depending on the grism<sup>2</sup>.

## 2.3. Adjustment of the Wavelength Scales

In order to obtain accurate flux calibrations, a precise wavelength scale must be established; but the extraction of a spectrum from its image is subject to small wavelength errors due to inaccuracies in either finding the zero order in the grism image or the stellar image on the reference direct image. When the zero order is off the grism image and no direct reference image is available, larger wavelength errors are expected. Therefore, the initial results are updated by comparison to spectral features in the overlap region with STIS between 0.8 and  $1.0 \mu\text{m}$  (for G102) or with a reference spectrum at longer wavelengths (for G141). For an A-star type spectrum, the strong Paschen and Brackett hydrogen series provide clean isolated lines with precisely known wavelengths.

## 2.4. Co-adding and Merging Individual Observations

All the separate G102 and G141 observations of a source are co-added and merged. The default merge point where the co-add switches from G102 to G141 is at  $11250 \text{ \AA}$ . The fluxes of the two independent measurements agree within the accuracy goal of 1% at the merge point.

## 3. THE CORRECTION FOR CHANGING SENSITIVITY

<sup>2</sup> At present, NICMOS is not an active HST instrument. See <http://www.stsci.edu/hst/nicmos>.

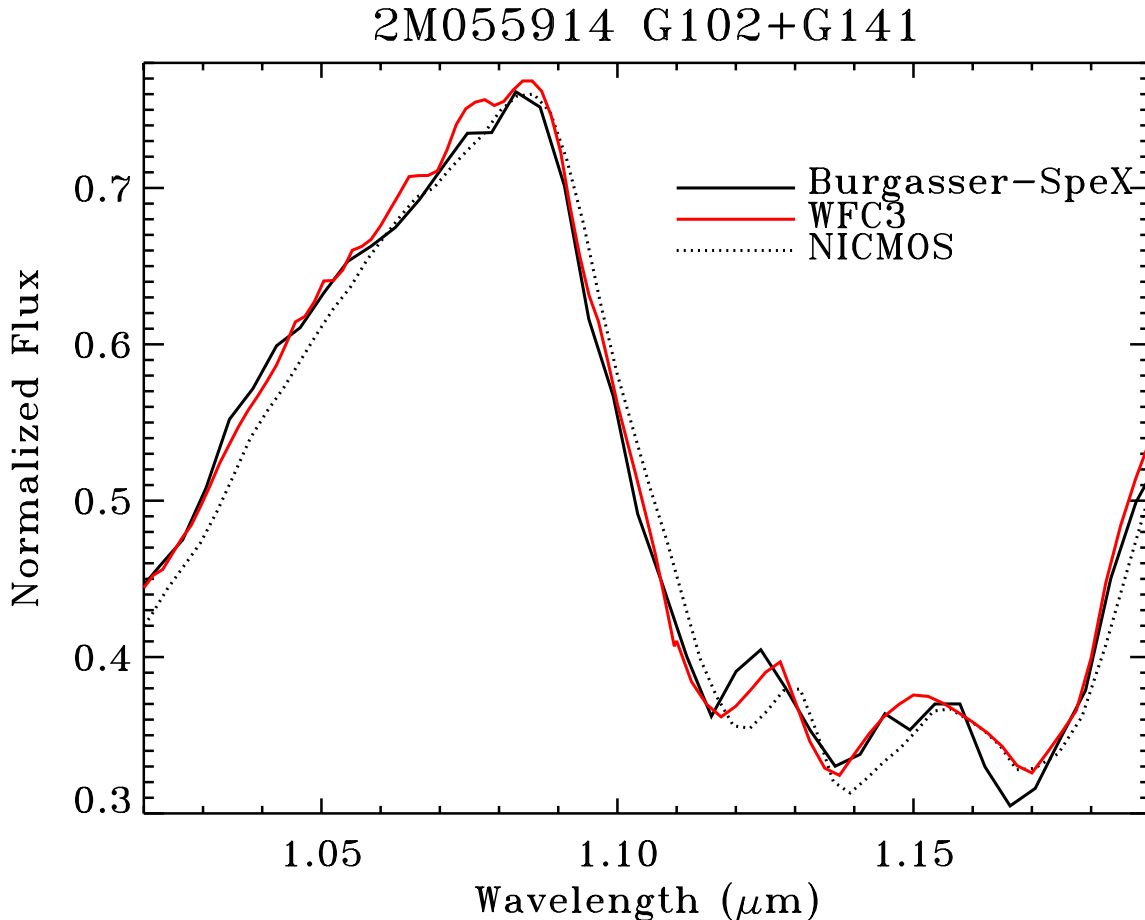


**Figure 1.** A section of the spectrum of 2M055914 from WFC3 (red) overplotted with the NICMOS spectrum (dotted) and SpeX data of (Burgasser et al. 2006) (solid black). The WFC3 agrees much better with SpeX, while NICMOS is shifted significantly toward longer wavelengths.

To investigate temporal sensitivity change, the spectral data of the four monitor stars, G191B2B, GD153, GD71, and GRW+70°5824, are binned over the regions of peak sensitivity from 8500–11300 Å for G102 and 11600–16000 Å for G141. For each monitor star, the individual bins are divided by their ensemble average. Figures 2 and 3 show all 177 ratios for G102 and all 174 ratios for G141 as a function of time. Linear least-square fits to the ratios give slopes of  $0.169 \pm 0.015\%$  per year for G102 and  $0.085 \pm 0.014\%$  per year for G141. The points in Figures 2 and 3 have small corrections for the non-linearity from the next section. These sensitivity changes are likely due to the polymerization of contaminants on the optical surfaces, which causes similar results for ACS (Bohlin et al. 2011), where the loss rates for the long wavelength filters F606W, F775W, and F814W are 0.26, 0.13, and 0.09%, per year respectively. For STIS, the low dispersion grating mode G750L shows losses in the range of 0.11–0.23% per year for the 5500–8300 Å wavelength range (Bohlin, unpublished).

These standard star observations are spaced over the whole detector, which means that the rms scatter includes uncertainties in the flat-field correction. The precision of stellar SEDs at the same position is slightly better. For example, the GRW+70°5824 observations are all within  $3.5''$  of center; and the rms scatter is 0.35 and 0.37% for G102 and G141, respectively, compared to 0.45% and 0.42% for the whole ensemble.

To check for a wavelength dependence of the sensitivity changes, a fit to the region 10000–11600 Å for G102 results in a slope of  $0.192 \pm 0.019\%$  per year, which agrees within  $\sim 1\sigma$  of the adopted 0.169% per year. These time-dependent sensitivity corrections are applied to the individual grism spectra extracted as described in Section 2.

As of 2018 December, the most recent set of WFC3 IR grism observations of the four monitor stars was 2017 Nov 11. Routine monitoring is needed for the valuable WFC3 grism modes. All four stars should be observed in both IR grism

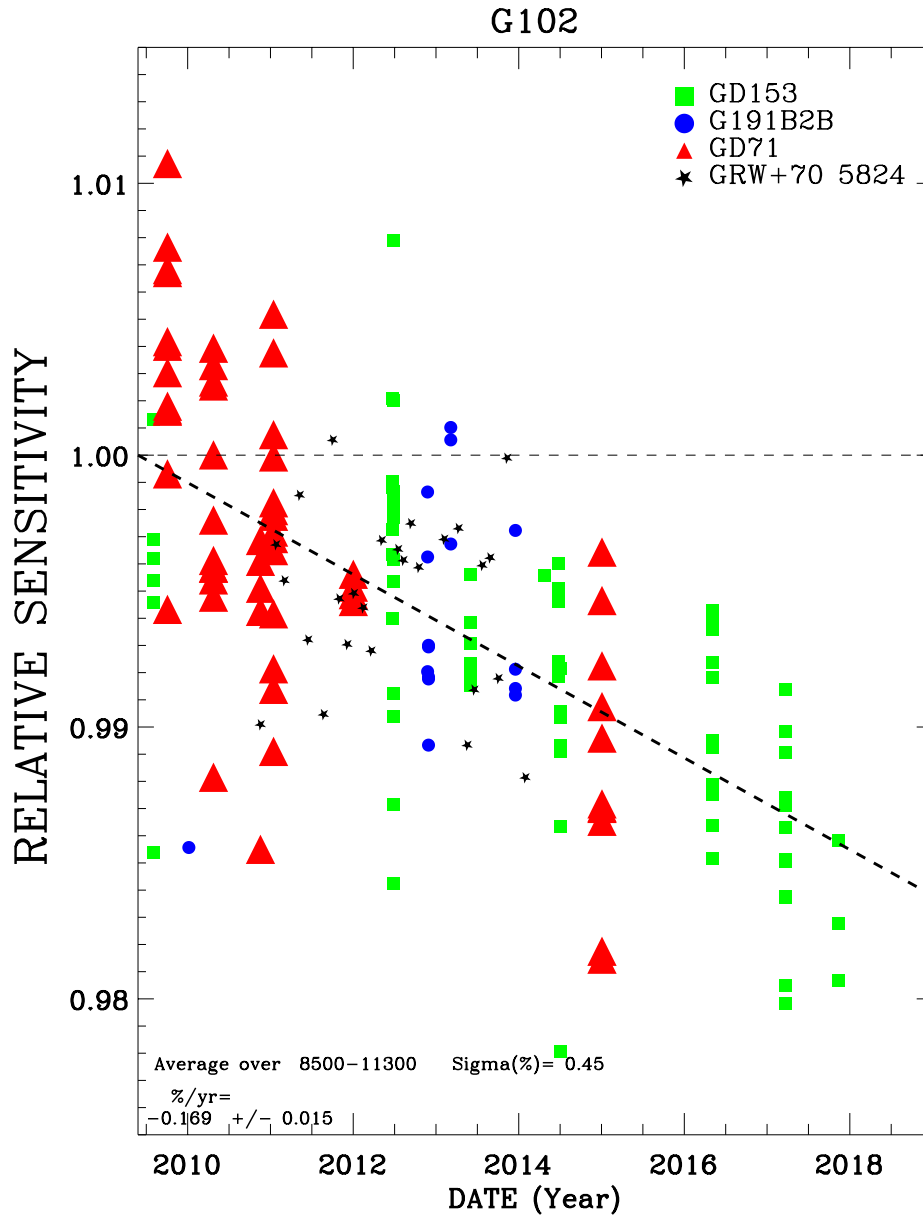


**Figure 2.** The change in sensitivity with time since 2009 for the WFC3 G102 grism after correction for non-linearity. The loss rate of  $0.169 \pm 0.015\% \text{ yr}^{-1}$  and the rms residual scatter of 0.45% are written near the bottom of the plot. The rms scatter is a measure of the repeatability, i.e. the  $1\sigma$  broadband uncertainty in an individual observation. The least square fit (dashed line) and the data points are all normalized to unity at 2009.4 by dividing by initial value of the fit at 2009.4.

modes every year, which is the cadence adopted by ACS for the most important filters; STIS sets the cadence at every two years. A standard reference position for the monitor stars improves the precision for absolute flux measurements on the IR detector.

#### 4. COUNT RATE NON-LINEARITY CORRECTION FOR THE WFC3 IR GRISM DATA

The WFC3 IR detector is a HgCdTe type, which is inherently non-linear. One type of non-linearity is the count-rate non-linearity correction (CRNL) found for NICMOS (Bohlin et al. 2005, 2006). CRNL should not be confused with the total count non-linearity, which occurs as the charge accumulated in a pixel approaches the detector full-well depth. The WFC3 HgCdTe detector is an improved version but still must be investigated for a corresponding non-linearity. In the case of NICMOS, the best measures of the non-linearity were from comparisons to STIS below  $1 \mu\text{m}$ , to WD model SEDs above  $1 \mu\text{m}$ , and to results from high background observations of P014C. However, WFC3 cannot superpose

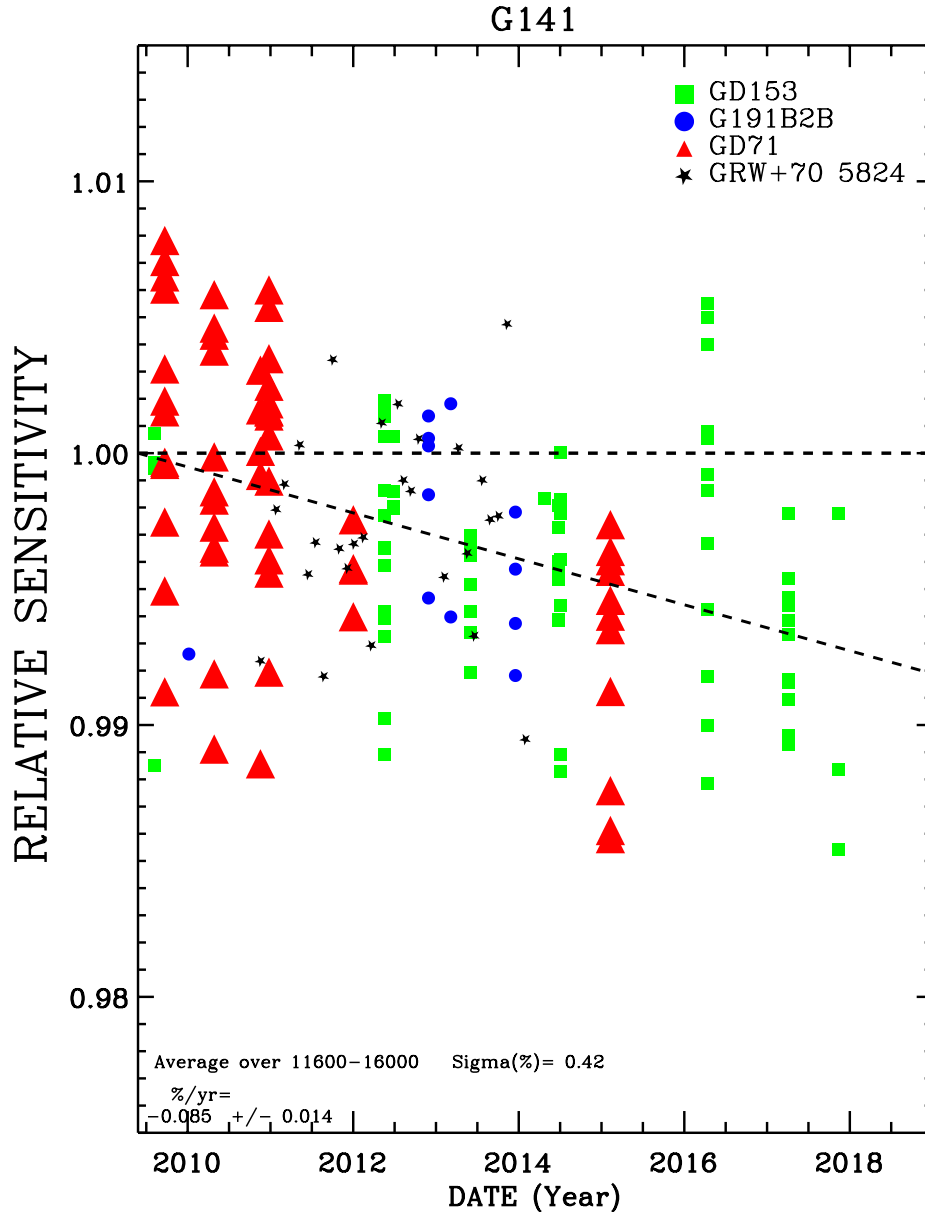


**Figure 3.** The change in sensitivity with time for the WFC3 G141 grism after correction for non-linearity. The loss rate of  $0.085 \pm 0.014\% \text{ yr}^{-1}$  and the rms scatter of 0.42% are written near the bottom of the plot. The rms scatter is a measure of the repeatability, i.e. the  $1\sigma$  broadband uncertainty in an individual observation. The least square fit (dashed line) and the data points are all normalized to unity at 2009.4.

lamp illumination on a stellar observation to raise the background, which limits the present analysis to comparisons of the grism data to STIS and to stellar atmosphere models that match the STIS SEDs.

In addition to the high-background result, the NICMOS CRNL measures relied heavily on models for the pure-hydrogen WDs WD1057+719 and WD1657+343 longward of  $1 \mu\text{m}$ . However, WD1057+719 is not observed, and only one observation of WD1657+343 exists in the present WFC3 IR grism dataset. The set of WFC3 IR SEDs could be compared to the overlapping set of NICMOS results, but the uncertainty in the NICMOS correction is greater than the total WFC3 CRNL. Instead, WFC3 data are corrected for sensitivity changes with time and then compared to stellar models that extend STIS observations into the IR using fits from the BOSZ stellar atmosphere grid (Bohlin et al. 2017). The models are fit to only the STIS data without using NICMOS or WFC3 as a constraint in the IR. Then, both the WFC3 and model SEDs are binned in  $500 \text{ \AA}$  bins, and the flux ratios of WFC3 IR grism to model are

plotted against the WFC3 net count rate in electrons  $s^{-1}$  for each bin.

An example of such a plot appears in Figure 4 for the 1–1.05  $\mu m$  bin. The slope of the least-square fit,  $1.00 \pm 0.28$  % per dex, is the measure of the CRNL, where the faint stars are too faint and the bright stars too bright by 1.00% for each factor of 10 in the count rate. While there is a moderate amount of scatter among the data points, the result for this one bin has a  $4\sigma$  level of significance.

**Figure 5 shows the CRNL for all 18 of the 500  $\text{\AA}$  bins as a function of the mean wavelength of each bin.** The error bars increase with wavelength, because the modeled extrapolations of the SEDs lose precision with increasing distance from the STIS anchor spectra below 1  $\mu m$ . Except for the one bin centered at 9250  $\text{\AA}$ , the count-rate non-linearity measures are all within  $1\sigma$  of the weighted mean value of  $0.72 \pm 0.08\%$  per dex.

**A recent analysis using IR photometry finds  $0.77 \pm 0.08$  mag per dex (Riess et al. 2019). Our result of  $0.72 \pm 0.08\%$  per dex from grism spectrophotometry corresponds to  $0.78$  mag per dex. As an unfortunate result of verbal communication, Riess et al. (2019) understood our result to be in mag units rather than percent. The independent Riess et al. (2019) result of  $0.77$  mag per dex from all photometry corresponds to  $0.71$  % per dex, and the average of the two independent analyses should be  $0.715$  % per dex or  $0.775$  mag per dex. For this work,  $0.72 \pm 0.06\%$  per dex is adopted for the average result.**

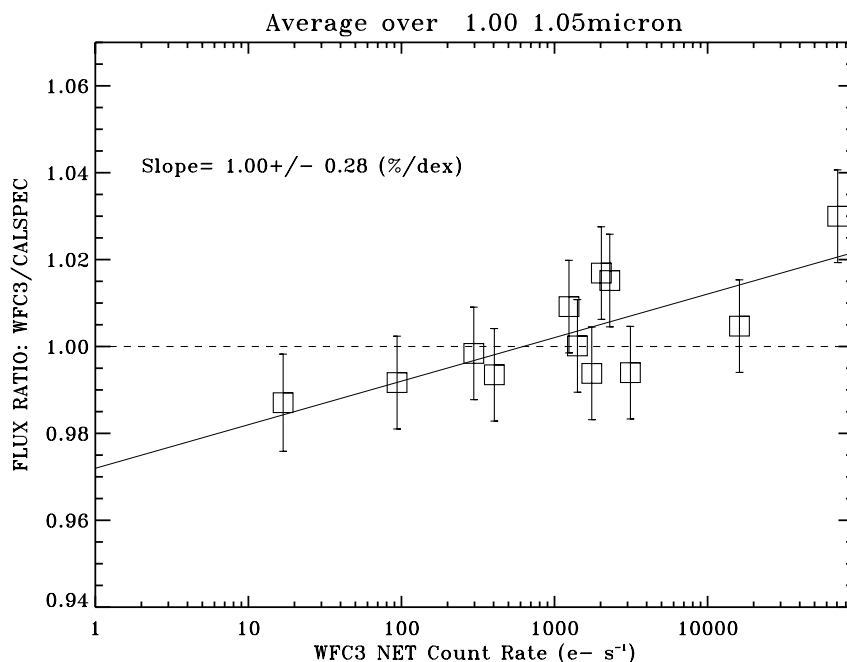


**Figure 4.** The WFC3 G102 CRNL for the 1–1.05  $\mu m$  wavelength bin from a comparison of the average grism SED with a model for each of the 12 stars. The models are independent of any NICMOS or WFC3 data. The line is the least square fit to the 12 data points and has a slope of  $1.00 \pm 0.28\%$  per dex. The uncertainties shown as error bars are dominated by the repeatability of the grism observations in a 500 $\text{\AA}$  bin.

Statistically, this average value of the CRNL has a high level of significance and is implemented in the WFC3 IR grism data processing as a correction from the measured net count rate  $N(\text{obs})$  to corrected  $N(\text{corr})$  as

$$N(\text{corr}) = \frac{N(\text{obs})}{1.0072^{\log(N(\text{obs})/1000)}} \quad (1)$$

where the observed count rate is divided by 1000 to make the correction near unity in the brightness range of the three primary WD reference SEDs.

## 5. THE ABSOLUTE FLUX CALIBRATION

Because the spectra are uniformly extracted with a height of six pixels, sensitivities, i.e. flux calibrations, are required only for this case. Extracted signals in electrons  $s^{-1}$  are compared with the SEDs of the primary standards G191B2B, GD153, and GD71 (Bohlin et al. 2014) to define the flux calibration  $S$  with units of electrons  $s^{-1}$  per  $[\text{erg s}^{-1} \text{cm}^{-2} \text{\AA}^{-1}]$ . The extracted signal is divided by  $S$  to get the absolute flux after correcting for the change in sensitivity with



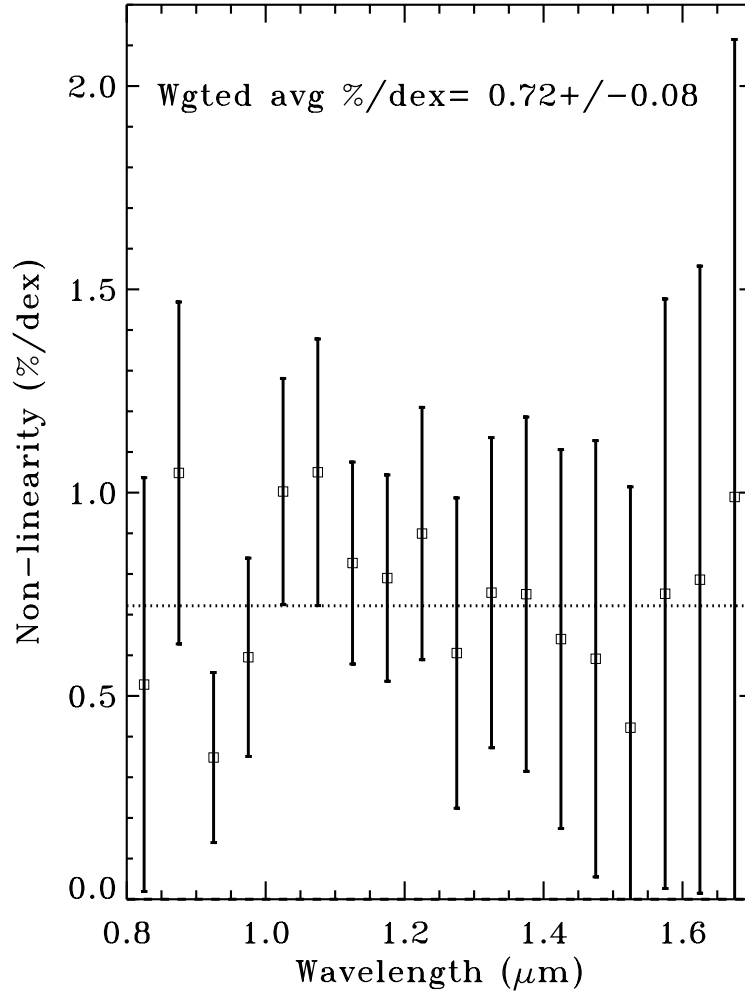


**Figure 5.** The WFC3 IR grism count rate non-linearity as a function of wavelength with  $1\sigma$  error bars. None of the results among the 18 bins of  $500 \text{ \AA}$  ( $0.05 \mu\text{m}$ ) width differs from the average of  $0.72 \pm 0.08 \text{ \% per dex}$  by as much as  $2\sigma$ , and only one bin differs by more than  $1\sigma$ . The data points are derived from comparisons of grism SEDs to models that are fit to STIS only, as in Figure 4.

time from Section 3 and for the CRNL from Section 4.

Each of the three primary standards has equal weight, and the ratio for each star to final average  $S$  is shown in Figure 6. The sensitivities at the strong  $P\beta$  line at  $12822 \text{ \AA}$  (vac) are interpolated across. The calibrations for the separate stars agree with their average to  $<1\%$  from  $8100\text{--}11500 \text{ \AA}$  for G102 and from  $10700\text{--}16600 \text{ \AA}$  for G141, which demonstrates consistency to  $<1\%$  in our merged fluxes from  $8100\text{--}16600 \text{ \AA}$ . The deviations of the curves from unity reflect the errors in the standard star SEDs combined with flat field errors that may cause inconsistent average signals due to the heterogeneous distributions of observation over the detector. Scatter near the ends of the wavelength ranges is caused by small wavelength errors and low signal that approaches the background level.

Table 2 collates the sensitivities  $S$  for G102 and G141, while Table 3 contains the resulting collection of new WFC3 IR grism SEDs.

## 6. EXTENDING THE SEDS INTO THE MID-IR FOR JWST CALIBRATION

### 6.1. Comparison of WFC3 to STIS and NICMOS SEDs

Differences between these new WFC3 IR results and NICMOS are the higher precision in the wavelength calibration (see Figure 1) and improved resolution for WFC3 IR compared to NICMOS. The biggest differences between the new WFC3 results and the NICMOS fluxes is for 2M055914, where Figure 1 illustrates some typical differences. Figure 7



compares the WFC3 and NICMOS SEDs to the model for P330E and shows the improved resolution of the WFC3 compared to NICMOS. Stellar absorption lines that match the model are evident in the WFC3 SED but not in the lower resolution NICMOS data. Visibility of stellar features enables essential adjustments to the wavelength vector to avoid wavelength errors that translate directly to flux errors.

Both the WFC3 and NICMOS flux distribution are compared to STIS in the overlap region at 8300–9700 Å where the *rms* deviations of the flux ratios from unity are 0.8% and 0.6% for NICMOS/STIS and WFC3/STIS, respectively. At the longer wavelengths, Figure 8 shows the ratios of NICMOS/WFC3 fluxes for the WFC3 G102 and G141 regions at 9000–11000 and 12000–16000 Å, respectively. The trends in Figure 8 suggest that the CRNL correction for NICMOS is underestimated by Bohlin et al. (2006), but only by  $\sim 0.8\%$  per dex in both wavelength regions. These errors of  $\sim 0.8\%$  per dex are within the uncertainties of the Bohlin et al. (2006) NICMOS non-linearity corrections of 4.8% per dex at 10000 Å and 2.6% per dex at 14000 Å.

### 6.2. Model Fits to SEDs with WFC3 Fluxes

Improvements to the model fits accrue from the improved WFC3 SEDs. Bohlin et al. (2017) modeled the nine K–A stars from Table 1 in order to extrapolate the observed HST SEDs to 32  $\mu\text{m}$  for JWST calibration. The new SEDs that include the WFC3 IR grism data are in CALSPEC and have been re-fit with the BOSZ model grid using the same chi-square ( $\chi^2$ ) technique as Bohlin et al. (2017). The search for a minimum  $\chi^2$  proceeds over the four parameters  $T_{\text{eff}}$ ,  $\log g$ ,  $\log z$ , i.e.  $[M/H]$ , and interstellar reddening from the dust  $E(B-V)$ . To calculate the best fit, the data are binned to avoid strong lines and regions of large line-blanketing, where the model calculations are less precise. The bins used by Bohlin et al. (2017) also avoided the NICMOS region below 1.3  $\mu\text{m}$ , where the non-linearity correction is the largest. However, the non-linearity correction for the WFC3 IR grisms is wavelength independent. The WFC3 wavelength bins used for cool and for hot stars appear in Table 4, and the new parameters of the model fits for nine stars appear in Table 5.

The biggest differences among the nine modeled IR SEDs are for C26202 and 1808347 with increases of  $\sim 1\%$  longward of 2  $\mu\text{m}$ . An example of the improvement over the model fit to only the STIS data appears in Figure 9 for 1808347. The BOSZ model parameters for the fit to the WFC3+STIS observations are in Table 5, while the STIS only fit parameters are  $T_{\text{eff}}=7910$  K,  $\log g=3.85$ ,  $[M/H]=-0.61$ , and  $E(B-V)=0.024$ . The red model fit is within 1% of the new WFC3 IR SED over most of its 1–1.7  $\mu\text{m}$  range. The old (green) model fit is more than 1% low with respect to the WFC3 data and with respect to the new model fit at the longer wavelengths.

**Table 2.** WFC3 IR Grism Flux Calibration  $S$

G102		G141	
Wavelength (Å)	$S^a$	Wavelength (Å)	$S^a$
7608.0000	1.288E+15	10000	8.590E+14
7624.0000	1.679E+15	10025	9.605E+14
7640.0000	2.107E+15	10050	1.047E+15
7656.0000	2.645E+15	10075	1.125E+15
7672.0000	3.422E+15	10100	1.191E+15
7688.0000	4.465E+15	10125	1.302E+15

$^a$ electrons  $\text{s}^{-1}$   $[\text{erg s}^{-1} \text{cm}^{-2} \text{Å}^{-1}]^{-1}$

NOTE—Table 2 is published in its entirety in a machine-readable format.

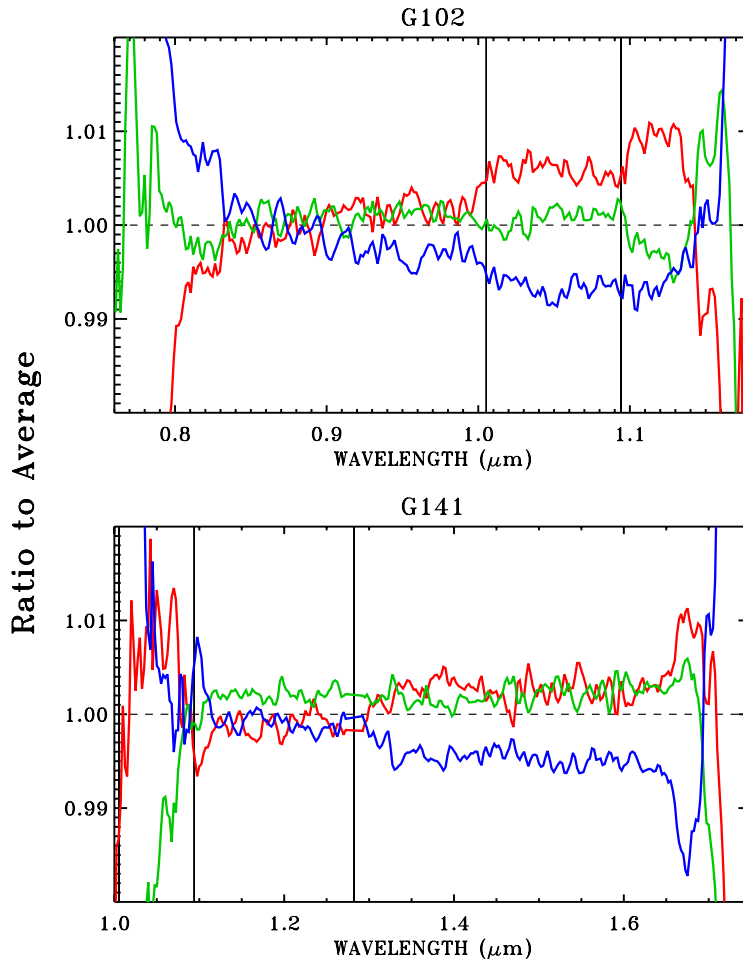


**Figure 6.** Ratio of the sensitivities for each of the primary standards to their average  $S$  for the IR grisms G102 and G141. Red-G191B2B, Green-GD153, Blue-GD71. Vertical lines mark the positions of the stronger absorption lines of hydrogen  $P\delta$ ,  $P\gamma$ , and  $P\beta$ , but notice the lack of spurious features in the sensitivities at those wavelengths.

**Table 3.** WFC3 IR SEDs for 19 Stars

Wavelength ( $\text{\AA}$ )	Net (electron $\text{s}^{-1}$ )	Flux <sup>a</sup>	Stat-err <sup>a</sup>	Sys-err <sup>a</sup>	No. Obs	Exp (s)
1757132						
7608.0	4.2500E+01	3.2997E-14	7.7682E-16	3.2997E-16	8	211.1
7624.0	5.5715E+01	3.3164E-14	6.2156E-16	3.3164E-16	8	211.1
7640.0	6.7358E+01	3.1954E-14	5.1542E-16	3.1954E-16	8	211.1
7656.0	8.3295E+01	3.1480E-14	4.2731E-16	3.1480E-16	8	211.1
7672.0	1.0848E+02	3.1683E-14	3.4880E-16	3.1683E-16	8	211.1
7688.0	1.4212E+02	3.1817E-14	2.8554E-16	3.1817E-16	8	211.1

<sup>a</sup> $\text{erg s}^{-1} \text{cm}^{-2} \text{\AA}^{-1}$

NOTE—Table 3 is published in its entirety in a machine-readable format which includes the SEDs for all 19 stars of Table 1. A portion for the star 1757132 is shown here for guidance regarding its form and content. Columns Stat-err and Sys-err are the statistical and 1% systematic uncertainty estimates.

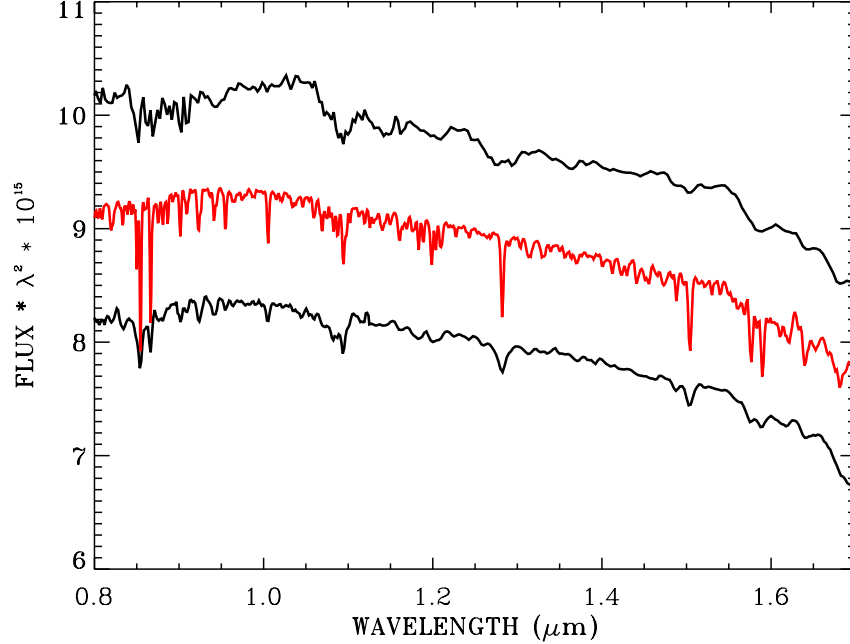


**Figure 7.** Comparison of the WFC3 IR SED to NICMOS for P330E. The BOSZ model for P330E is shown in red, while the WFC3 (below) and NICMOS (above) fluxes are multiplied by 0.9 and 1.1, respectively. Notice the good correspondence between the spectral features for the model and WFC3 SED, while the correspondence is poor for the NICMOS data. **The units of the Y-axis are the flux in  $10^{-15} \text{ erg s}^{-1} \text{ cm}^{-2} \text{ \AA}^{-1}$  multiplied by the wavelength squared in  $\mu\text{m}$  to flatten the traces.**

## 7. CONCLUSIONS

The newly derived WFC3 IR grism SEDs have uncertainties of  $\sim 1\%$  based on their agreement with the STIS flux distributions. These improved WFC3 IR flux distributions have more accurate models and increase confidence that the models represent the true stellar SEDs to  $32 \mu\text{m}$  with an *rms* precision approaching 1–2%. All of the CALSPEC SEDs should be upgraded to include WFC3 IR grism fluxes, especially those stars that are currently lacking NICMOS coverage or have noisy NICMOS SEDs. **The more accurate SEDs of the CALSPEC stars help to better constrain the parameters of the dark energy, where an absolute color calibration of better than 1% is required to improve current results.**

## ACKNOWLEDGEMENTS

Scott Fleming entered our HLSP into MAST. Support for this work was provided by NASA through the Space Telescope Science Institute, which is operated by AURA, Inc., under NASA contract NAS5-26555. This research made use of the SIMBAD database, operated at CDS, Strasbourg, France.

## ORCID iDs

Ralph C. Bohlin <https://orcid.org/0000-0001-9806-0551> and Susana E. Deustua <https://orcid.org/0000-0003-2823-360X>

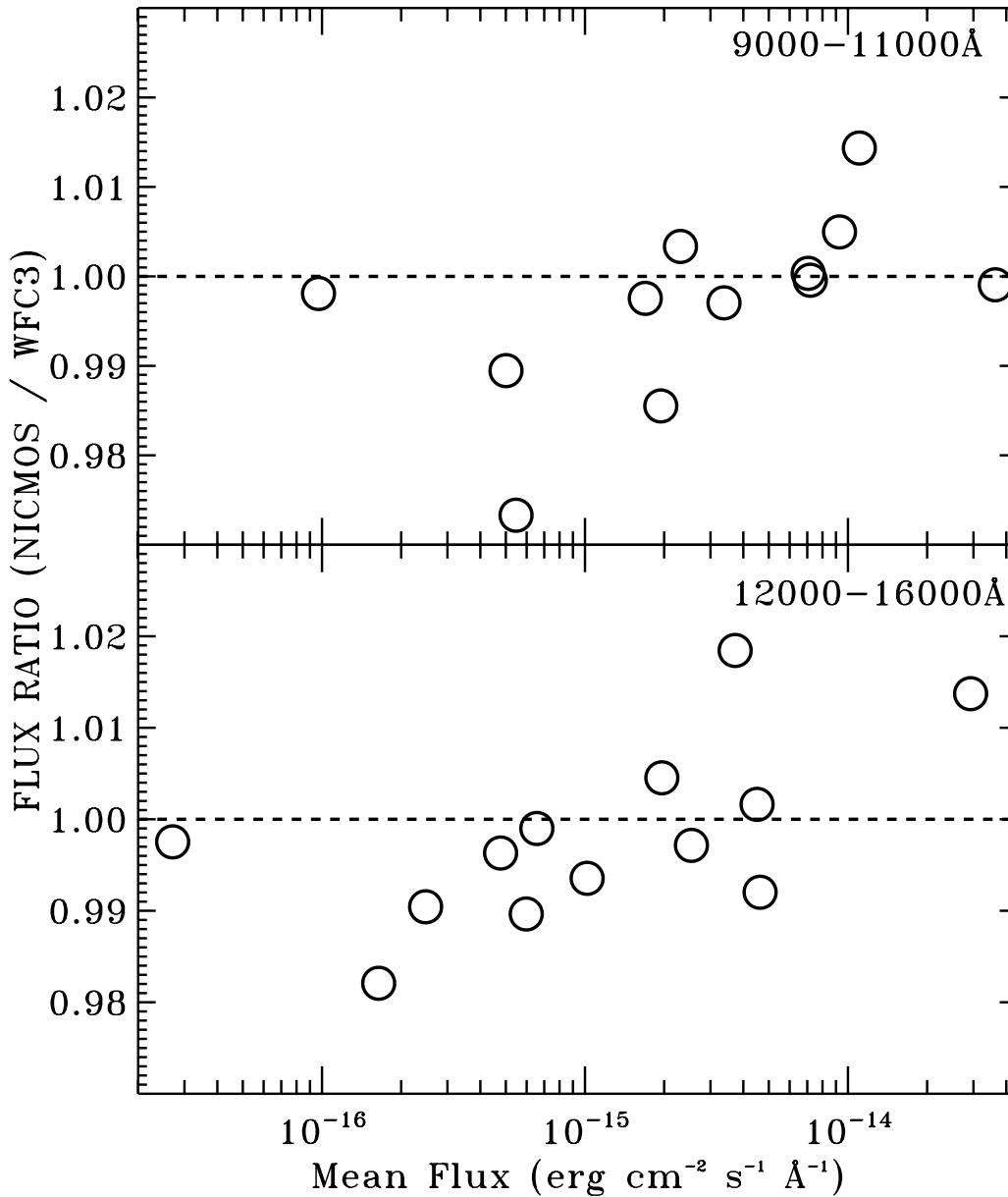


Figure 8. Ratio of NICMOS to WFC3 fluxes for G102 (upper panel, 12 stars) and G141 (lower panel, 13 stars). The flux for each star is averaged over the broad bands of 9000-11000 Å for G102 and over 12000-14000 Å for G141. The X-axis is the same average WFC3 flux used for the denominator of the ratios.

#### REFERENCES

- Albrecht, A., Bernstein, G., Cahn, R., et al. 2006, ArXiv Astrophysics e-prints, astro-ph/0609591
- Bohlin, R., Deustua, S. E., & Pirzkal, N. 2015, IR Grism Wavelength Solutions Using the Zero Order Image as the Reference Point, Tech. rep.
- Bohlin, R. C., Gordon, K. D., & Tremblay, P.-E. 2014, PASP, 126, 711 (B14)
- Bohlin, R. C., Lindler, D. J., & Riess, A. 2005, Grism Sensitivities and Apparent Non-Linearity, Instrument Science Report, NICMOS 2005-02, (Baltimore: STScI), Tech. rep.
- Bohlin, R. C., Mack, J., & Ubeda, L. 2011, Flux Calibration of the ACS CCD Cameras III. Sensitivity Changes over Time, Instrument Science Report, ACS 2011-03, (Baltimore: STScI), Tech. rep.
- Bohlin, R. C., Mészáros, S., Fleming, S. W., et al. 2017, AJ, 153, 234
- Bohlin, R. C., Riess, A., & de Jong, R. 2006, NICMOS Count Rate Dependent Non-Linearity in G096 and G141, Instrument Science Report, NICMOS 2006-02, (Baltimore: STScI), Tech. rep.
- Burgasser, A. J., Geballe, T. R., Leggett, S. K., Kirkpatrick, J. D., & Golimowski, D. A. 2006, ApJ, 637, 1067

Cushing, M. C., Vacca, W. D., & Rayner, J. T. 2004,

Publications of the Astronomical Society of the Pacific, 116,  
362

Holberg, J. B., Bergeron, P., & Gianninas, A. 2008, *AJ*, 135, 1239

Kuntschner, H., Bushouse, H., Kümmel, M., & Walsh, J. R.

2009a, WFC3 SMOV proposal 11552: Calibration of the G102  
grism, Tech. rep.

—. 2009b, WFC3 SMOV proposal 11552: Calibration of the  
G141 grism, Tech. rep.

Pirzkal, N., Ryan, R., & Brammer, G. 2016, Trace and  
Wavelength Calibrations of the WFC3 G102 and G141 IR  
Grisms, Tech. rep.

Riess, A. G., Narayan, G., & Calamida, A. 2019, Calibration of  
the WFC3-IR Count-rate Nonlinearity, Sub-percent Accuracy  
for a Factor of a Million in Flux, Tech. rep.

Scolnic, D., Rest, A., Riess, A., et al. 2014, *ApJ*, 795, 45

Stubbs, C. W., & Brown, Y. J. 2015, *Modern Physics Letters A*,  
30, 1530030

Stubbs, C. W., & Tonry, J. L. 2016, in *Astronomical Society of  
the Pacific Conference Series*, Vol. 503, *The Science of  
Calibration*, ed. S. Deustua, S. Allam, D. Tucker, & J. A.  
Smith, 37

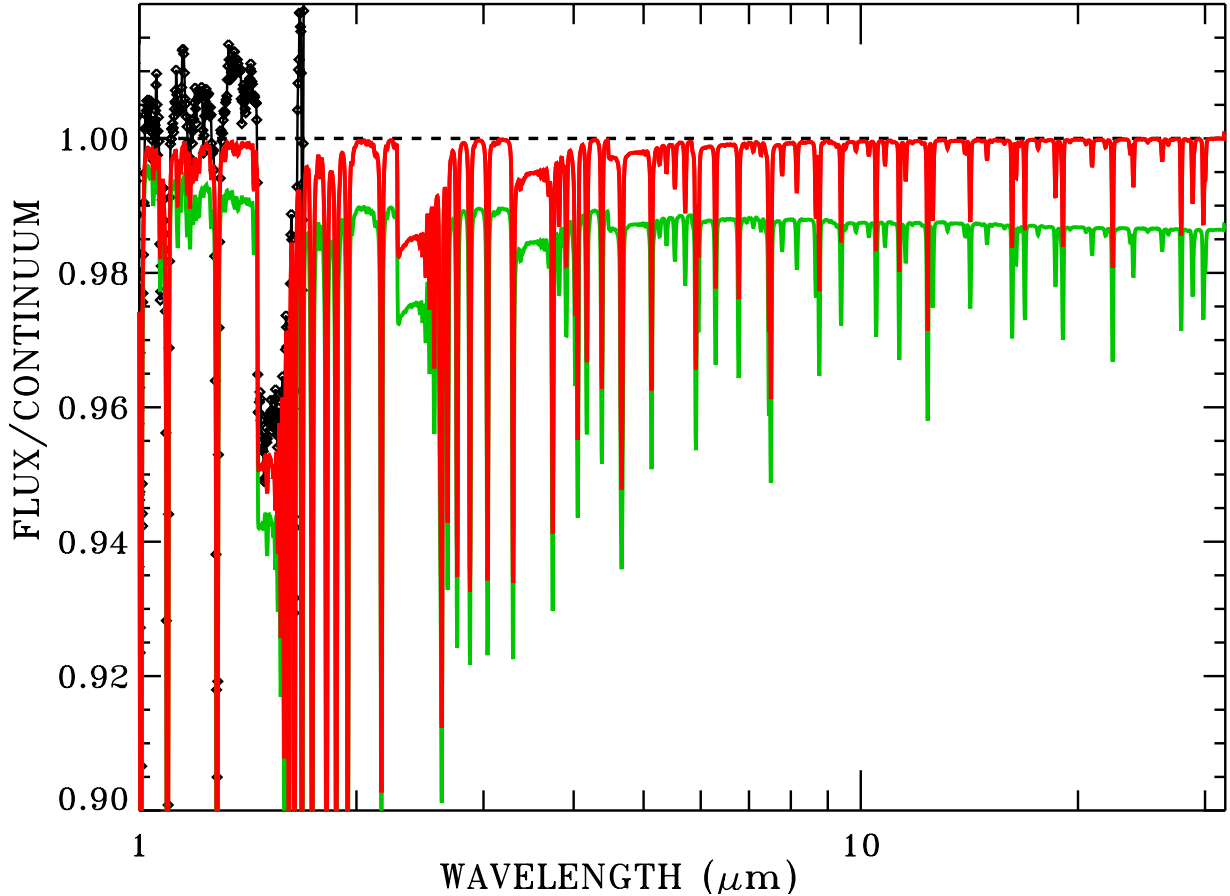


**Figure 9.** Black data points: WFC3 IR grism flux at 1–1.7  $\mu\text{m}$  for 1808347. Red: BOSZ model fit to the STIS+WFC3 SED. Green: BOSZ model fit to just the STIS SED. Fluxes for all three spectral traces are divided by the same model continuum for the red fit to the STIS+WFC3 SED in order to illustrate differences at the 1% level. The WFC3 SED and its red fit agree within 1% over most of the observed range. At the longer wavelengths, the green fit to STIS alone is more than 1% lower than the improved red fit to the full SED that includes the new WFC3 IR grism results.

**Table 4.** Broad Bands in Å for Fitting Stellar Models to STIS and WFC3 Grism-IR SEDs

K-G-F Stars	A-B-O Stars
	1280–1510
	1725–2020
	2110–2280
	2520–2780
3000–3850	3000–3200
4000–4260	3200–3400
4380–4800	3400–3640
4950–5500	3750–4400
5500–6000	4400–4800
6000–6500	4950–5500
6620–7400	5500–6000
7400–8400	6000–6500
8800–9400	6620–7400
9400–10000	7400–7900
10200–10750	7900–8200
11100–12600	9182–9282
13000–14150	9290–9480
14150–15300	9499–9599
	9600–10000
	10200–10750
	11100–12600
	13000–14150
	14150–15300

NOTE—These wavelength bands are used for averaging the observed and model fluxes into bins for fitting models from the BOSZ grid according to the method of [Bohlin et al. \(2017\)](#) that minimizes  $\chi^2$  over four parameters.

**Table 5.** Parameters of the Model Fits

Star	$T_{\text{eff}}$	$\log g$	$[M/H]$	E(B-V)	$\chi^2$
1757132	7540	3.65	0.12	0.023	1.14
1802271	9060	4.00	-0.47	0.019	0.99
1808347	7860	3.80	-0.74	0.022	3.06
BD+60°1753	9330	3.90	-0.13	0.009	0.93

*Table 5 continued on next page*

Table 5 (*continued*)

Star	$T_{\text{eff}}$	$\log g$	$[M/H]$	E(B-V)	$\chi^2$
C26202	6270	4.40	-0.46	0.067	0.23
HD37725	8420	4.30	-0.08	0.049	1.37
KF06T2	4500	1.55	-0.26	0.050	0.32
P330E	5810	4.95	-0.22	0.025	0.40
SNAP2	5700	4.25	-0.21	0.024	0.08

NOTE—Results from fitting BOSZ model atmospheres to the observed stellar SEDs using the method of [Bohlin et al. \(2017\)](#) and the wavelength bins of Table 4. The parameters of the fit for each star are the effective temperature  $T_{\text{eff}}$ , the surface gravity  $\log g$ , the metallicity  $[M/H]$ , the interstellar reddening E(B-V), and the chi-square quality of the fit  $\chi^2$ .